

Structural Description of the $\text{Na}_2\text{B}_4\text{O}_7$ – Na_3AlF_6 – TiO_2 System. 2. A Multinuclear NMR Approach of Melts and Solids

Pierre Florian,[†] Elena M. Anghel,[‡] and Catherine Bessada^{*,†}

Centre de Recherche sur les Matériaux à Haute Température, CRMHT-CNRS, 1D, Avenue de la Recherche Scientifique, 45071 Orléans, Cedex 2, France, and Institute of Physical Chemistry “Ilie Murgulescu” of Romanian Academy, Spl. Independentei 202, 060021 Bucharest, Romania

Received: August 11, 2006; In Final Form: November 16, 2006

A quantitative structural investigation of pseudo-binary $\text{Na}_2\text{B}_4\text{O}_7$ – $[\text{Na}_3\text{AlF}_6\text{–TiO}_2]_{11}$ was carried out by NMR spectroscopy. We applied high-resolution solid-state NMR on quenched samples and in situ high-temperature NMR spectroscopy on molten compositions to obtain a more accurate description of the melts. Consistent with our previous findings, two compositional ranges can be evidenced. Below 50 mol % $\text{Na}_2\text{B}_4\text{O}_7$, the $\text{Ti}^{\text{IV}} \rightarrow \text{Ti}^{\text{VI}}$ valence conversion prevails, leading to the formation of $\text{B}(\text{O},\text{F})_3$ species at the expense of $\text{B}(\text{O},\text{F})_4$ ones and a low average coordination number of aluminum; above 50 mol %, the system behaves mainly like the binary $\text{Na}_2\text{B}_4\text{O}_7$ – Na_3AlF_6 where Na_3AlF_6 is playing a network former role. The dominant oxyfluoro-species evidenced by double-resonance NMR in the quenched samples are BO_2F_2 , BO_3F , BO_2F , BOF_2 , NaO_7F , NaO_6F_2 , and AlO_4F with sodium in various coordination states, $\text{Na}(\text{O},\text{F})_8$, $\text{Na}(\text{O},\text{F})_7$, and $\text{Na}(\text{O},\text{F})_6$. F–Ti bonds were found to be almost negligible whereas F– Al_2 , F–B, F–Na, and F–Al–Na bonds were clearly observed in the solid state.

1. Introduction

The quaternary NaCl – Na_3AlF_6 – $\text{Na}_2\text{B}_4\text{O}_7$ – TiO_2 carries a high practical interest because it could be used for industrial production of high purity TiB_2 ^{1,2} powders. This production would be achieved by a high-temperature electrosynthesis process involving a high-temperature melt in which chemical reactions between the $\{\text{NaCl}, \text{Na}_3\text{AlF}_6\}$ solvent and the $\{\text{Na}_2\text{B}_4\text{O}_7, \text{TiO}_2\}$ electroactive component occur. It is therefore of great importance to investigate this system in situ in the molten phase, starting with less complex subsystems like the binary Na_3AlF_6 – $\text{Na}_2\text{B}_4\text{O}_7$ system already investigated³ or the ternary Na_3AlF_6 – $\text{Na}_2\text{B}_4\text{O}_7$ – TiO_2 system, which is the subject of this work. The effect of NaCl addition over the ternary melts will be the subject of a forthcoming study.

High-temperature NMR spectroscopy⁴ has already proven to be a valuable tool to investigate high-temperature molten salts.^{5–7} It has been previously applied in our laboratory³ on the binary $\text{Na}_2\text{B}_4\text{O}_7$ – Na_3AlF_6 and is now extended to the pseudo-binary $\text{Na}_2\text{B}_4\text{O}_7$ – $[\text{Na}_3\text{AlF}_6\text{–TiO}_2]_{11}$ (11 stands for the fixed wt % of TiO_2 in the Na_3AlF_6 – TiO_2 system). We chose 11% (recalling that the eutectic composition corresponds to 3.5%) and varied the relative proportions between $\text{Na}_2\text{B}_4\text{O}_7$ and $[\text{Na}_3\text{AlF}_6\text{–TiO}_2]_{11}$, keeping in mind that the TiB_2 powders were obtained only for an atomic B/Ti ratio from 12 to 20.

Moreover, high-resolution solid-state NMR techniques were extensively employed for the study of disordered materials and are suitable for glass forming borates. Double resonance techniques such as REDOR⁸ can be applied to probe the connectivity between the different cations (²⁷Al, ²³Na, ¹¹B) on

TABLE 1: Nominal Compositions, Melting Temperature, and Atomic Ratio B/Ti for the Pseudo-binary Samples: $\text{Na}_2\text{B}_4\text{O}_7$:[$\text{Na}_3\text{AlF}_6\text{–TiO}_2$]₁₁^a

sample	T_m °C	$\text{Na}_2\text{B}_4\text{O}_7$: Na_3AlF_6 : TiO_2 wt %	$\text{Na}_2\text{B}_4\text{O}_7$: Na_3AlF_6 : TiO_2 % mol	B/Ti
0T11	985	0:89:11	0:75.49:24.51	0
20T11	923	20:71.2:8.8	18.11:61.82:20.07	3.60
40T11	895	40:55.4:6.6	37.22:47.38:15.40	9.66
50T11	880	50:44.5:5.5	46.94:40.04:13.02	14.42
60T11	847	60:35.2:4.4	57.03:32.43:10.54	21.64
80T11	690	80:17.8:2.2	77.96:16.62:5.42	57.53
100T11	742	100:0:0	100:0:0	

^a Melting temperatures were obtained from DTA curves (MOM-Budapest apparatus, 10 °C/min rate).

one hand and the two anions, ¹⁷O and ¹⁹F, on the other hand in oxyfluoro-species. A qualitative description of the medium-range order with the formation of $\text{B}(\text{O},\text{F})_4$ and $\text{B}(\text{O},\text{F})_3$ units has been inferred from our previous IR and Raman data,⁹ and a more precise characterization can be expected through these NMR techniques. Those investigations on the glassy part of the solidified samples is the only insight one can gain on the possible “structure” of the melts, despite the fact that almost all samples contain crystallites embedded in a glassy matrix.

2. Experimental

As previously described,⁹ NaBF_4 and Na_2TiF_6 (Acros, 98% of purity and all reagent grade), Na_3AlF_6 (Merck), TiO_2 (Merck), and $\text{Na}_2\text{B}_4\text{O}_7 \cdot 10\text{H}_2\text{O}$ (Reactivul Bucharest) were used as starting materials. Anhydrous $\text{Na}_2\text{B}_4\text{O}_7$ was prepared from Borax as reported elsewhere.³

The various mixtures (see Table 1), $\text{Na}_2\text{B}_4\text{O}_7$ – $[\text{Na}_3\text{AlF}_6\text{–TiO}_2]_{11}$, were prepared by conventional melt methods and stored in a drybox, as described in our previous study.⁹ All compositions are represented by wt % throughout this paper unless specified otherwise.

* Corresponding author. E-mail: bessada@cnrs-orleans.fr. Fax: +33-(0) 238 638 103.

[†] Centre de Recherche sur les Matériaux à Haute Température.

[‡] Institute of Physical Chemistry “Ilie Murgulescu” of Romanian Academy.

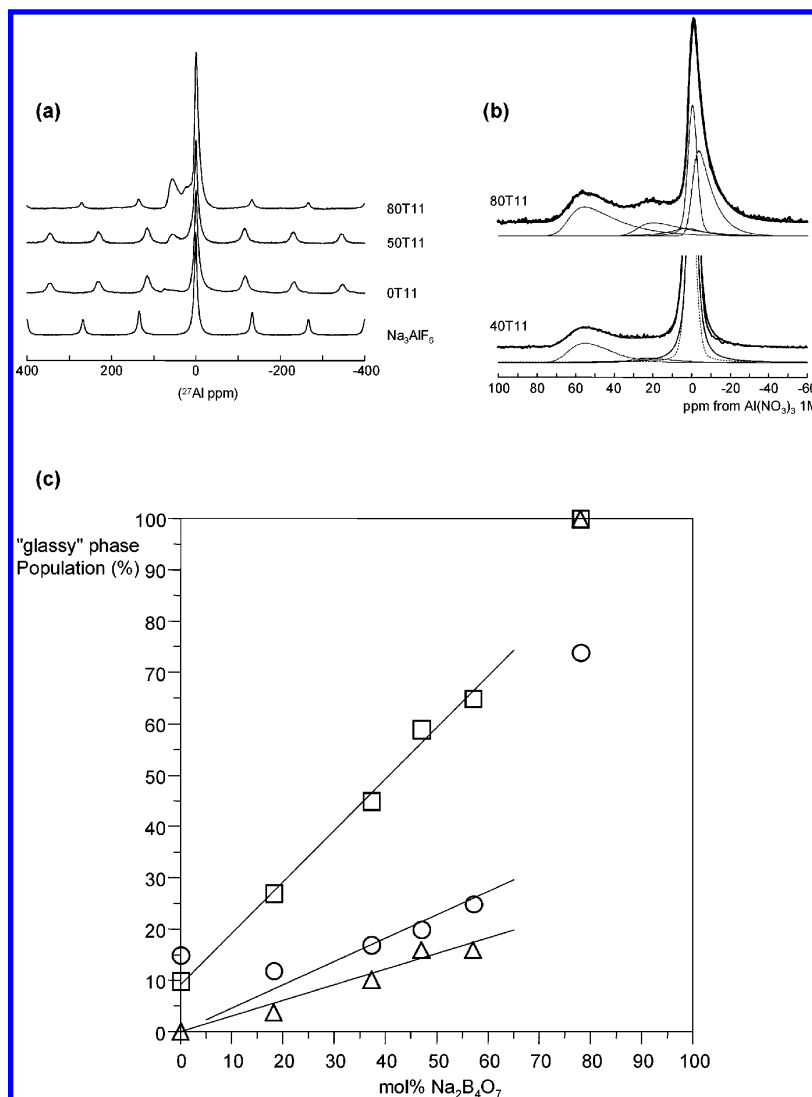


Figure 1. (a) Stack plot of selected ^{27}Al MAS NMR spectra in the $\text{Na}_2\text{B}_4\text{O}_7$ – $[\text{Na}_3\text{AlF}_6\text{-TiO}_2]_{11}$ mixtures along with reference samples: 0T11 ($\text{Na}_3\text{AlF}_6\text{:TiO}_2 = 89\text{:}11$) and Na_3AlF_6 . (b) Simulation of the ^{27}Al MAS spectrum obtained for 40T11 (bottom, the dashed line represents the $n = 0$ spinning sideband) and 80T11 (top). (c) Compositional dependence of the disordered borate phase population obtained from the ^{23}Na (squares), ^{27}Al (circles), and ^{19}F (triangles) spectra. Linear regressions are only a guide for the eyes.

NMR experiments have been carried out using a Bruker DSX 400 NMR spectrometer, operating at 128.3, 104.2, 105.8, and 376.4 MHz for ^{11}B , ^{27}Al , ^{23}Na , and ^{19}F , respectively. For solid-state ^{11}B experiments, we also took advantage of the peak separation obtained at high fields and used a 17.6 T spectrometer operating at 240.6 MHz. Chemical shifts were externally referenced to a 1 M aqueous solution of $\text{Al}(\text{NO}_3)_3$, a 1 M aqueous solution of NaCl , $(\text{C}_2\text{H}_5)_2\text{OBF}_3$, and CFCl_3 for ^{27}Al , ^{23}Na , ^{11}B , and ^{19}F , respectively.

All high-temperature static spectra were acquired using a single pulse sequence, with $\pi/2$ pulses, a recycle delay of 1 s and 8 to 128 accumulations, using a CO_2 -laser heating system developed in our laboratory.⁷ Samples, filled in a tight-closed BN crucible under dried argon (70–75 mg each), were heated up directly above their melting points (see Table 1) at 1030 °C no longer than 5 min to limit evaporation. ^{23}Na and ^{27}Al spectra were recorded in succession; ^{19}F and ^{11}B spectra were obtained from a fresh sample under the same conditions. In order to prevent Ti^{4+} reduction to Ti^{3+} as well as a possible reaction between the sample and the boron nitride crucible at high temperature, the inner part of the BN cell was protected with one or two zirconia coatings. In situ ^{11}B spectra required correction from a broad probe-head signal due to the presence

of boron in the crucible material (BN) as well as in the probe assembly. The temperatures reported below are accurate within ± 5 °C.

Room-temperature magic angle spinning (MAS) NMR spectra were acquired with a high-speed MAS NMR probe (Bruker) with spinning speeds ranging from 20 to 35 kHz. ^{11}B , ^{27}Al , and ^{23}Na spectra were collected with an rf power of $\nu_{\text{rf}} = 50$ kHz, short excitation pulses of 0.5 μs (i.e., less than $\pi/2I(2I + 1)$ for quantitative measurements), recycle delays of 1 s, spectral widths of 1 MHz and typically 1024 scans. ^{19}F high power ($\nu_{\text{rf}} = 150$ kHz) two-pulse phase modulation (TPPM) decoupling was needed for ^{23}Na and ^{27}Al acquisitions, and it appeared to have no effect on ^{11}B lines. Owing to a long fluorine relaxation time in cryolite, ^{19}F one-pulse experiments were performed with a pulse flip angle of 10° ($\nu_{\text{rf}} = 70$ kHz), a recycle delay of 3 s, and 1024 scans. ^{19}F Hahn-echo sequences were applied at 105 rotor periods while spinning at 35 kHz (i.e., a 1 ms echo shift) with 512 scans and a recycle delay of 50 s (adjusted to the 35 s spin–lattice relaxation time of the amorphous component of the spectrum).

The isotropic chemical shifts, δ_{iso} , and the quadrupolar parameters (quadrupole coupling constant, C_Q , asymmetry parameter, η), characteristic of the different quadrupolar nuclei

TABLE 2: ^{27}Al NMR Parameters of Aluminum Sites Resulting from Simulations

sample				δ_{iso} ppm	$\Delta\nu_{1/2}$ kHz	ν_Q kHz	$\sigma(\nu_Q)$ kHz	%				assignment
80T11				65.9		874	568	28				Al^{IV}
				30.3		860	530	12				Al^{V}
				-0.3		524	445	33				Al^{VI}
				2.4	578	335 ^a		26				AlF_6
60T11 50T11 40T11 20T11				67.5		820	300	17	15	14	10	Al^{IV}
				35.5		820	300	8	5	2	2	Al^{V}
				0.0	330	140 ^a		75	80	83	88	AlF_6
0T11				81	300	1150	530	15				Al^{IV}
				-0.2	408	135 ^a		85				AlF_6

^a $\nu_{Q,\eta} = \nu_Q \sqrt{1 + \eta^2/3}$ (kHz) extracted from the position of the $n = 0$ spinning sideband of the external $\langle -3/2, 3/2 \rangle$ transition with respect to the position of the $\langle -1/2, 1/2 \rangle$ central transition.¹³

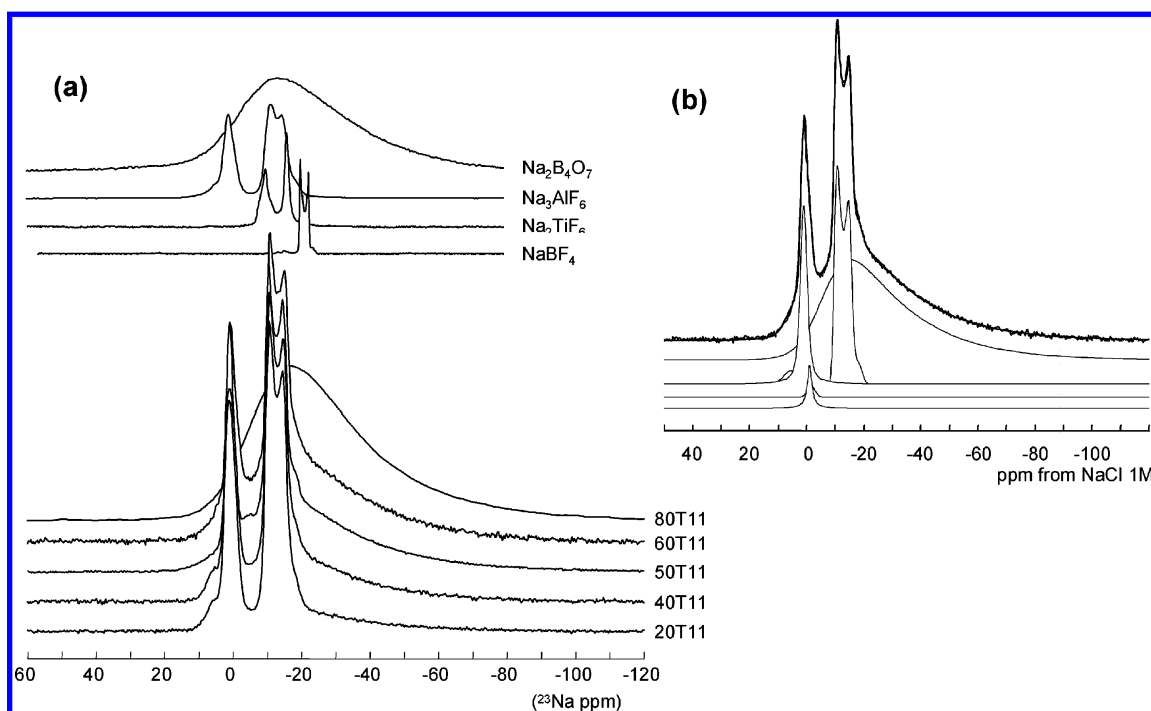


Figure 2. (a) Stack plot of ^{23}Na MAS NMR spectra of the various $\text{Na}_2\text{B}_4\text{O}_7$ – $[\text{Na}_3\text{AlF}_6\text{–TiO}_2]_{11}$ mixtures along with some reference compounds. (b) Simulation for the 40T11 sample of the ^{23}Na MAS spectrum.

under investigation, aluminum, sodium, and boron, as well as the relative population of the boron bearing units, B^{III} and B^{IV} , were calculated according to previously discussed protocols, employing the laboratory-developed software Dmfit.¹⁰

$\{^{19}\text{F}\}^{23}\text{Na}$ and $\{^{19}\text{F}\}^{11}\text{B}$ REDOR NMR experiments were carried out with spinning frequencies of 25 and 30 kHz, at a radio frequency field of 12.5 kHz (typical $\pi/2$ pulse lengths of 10 μs) for both ^{23}Na and ^{11}B , and a rf field of 70 kHz for ^{19}F . A standard pulse sequence as reported by Bertmer et al.¹¹ was used for collecting REDOR data. Recycle delays were adjusted to a few seconds according to the measured relaxation times of ^{23}Na and ^{11}B . For each slice, 256 to 1024 scans were accumulated for ^{23}Na and 16 to 64 scans for ^{11}B ; 64 and 32 pairs of (S , S_0) signals (S_0 is the reference signal and S is the attenuated signal for each scan) were acquired with time increments of rotor periods of 1 and 10 and 3 and 9, respectively.

3. Results and Discussion

3.1. Ex Situ High-Resolution Solid-State NMR. Aluminum-27. The ^{27}Al MAS NMR spectra of selected compositions in the $\text{Na}_2\text{B}_4\text{O}_7$ – $[\text{Na}_3\text{AlF}_6\text{–TiO}_2]_{11}$ system are displayed in Figure

1a. Our simulations of these partially resolved spectra were successfully performed by using three components (see Figure 1b) except for the glassy 80T11, which requires an additional “amorphous” line (Table 2). A clearly Gaussian-type line can be observed around 0 ppm with its associated spinning sideband manifold, corresponding to an aluminum environment experiencing a small electric field gradient (EFG) and for which only reduced quadrupolar parameters can be extracted from the position of the $n = 0$ spinning sidebands.¹² The broad and asymmetric component centered around 55 ppm represents an ensemble of aluminum sites experiencing a strong EFG and can be well simulated with a Gaussian distribution of quadrupolar parameters.¹³ Upon inspection, a second broad component is needed around 20 ppm to account for some intensity present in this region (also a third one at around 0 ppm for 80T11).

By analogy with the spectrum obtained for Na_3AlF_6 and in agreement with the behavior under ^{19}F decoupling, the sharp Gaussian line is attributed to fully fluorinated AlF_6^{3-} environments. This is related to the XRD data,⁹ which show that the only aluminum-containing crystalline phase is Na_3AlF_6 in all samples except 80T11, which is entirely vitreous. This strong

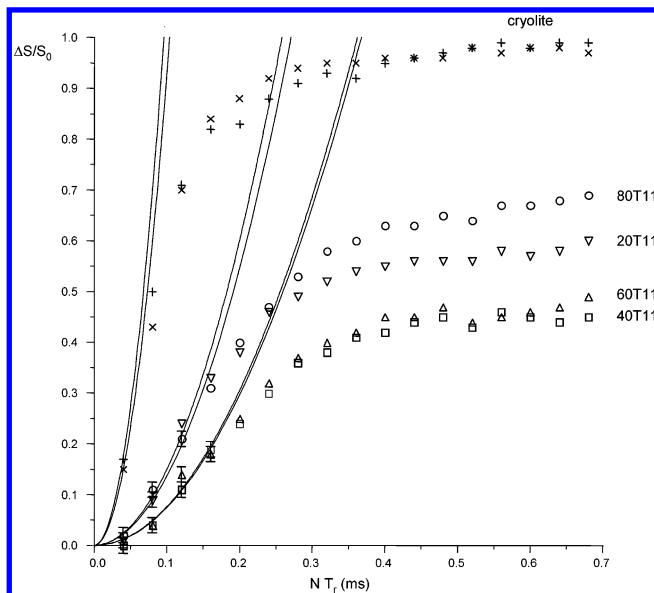
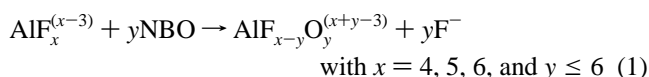


Figure 3. $\{^{19}\text{F}\}^{23}\text{Na}$ REDOR curves of the glassy contribution for 20T11 (triangles down), 40T11 (squares), 60T11 (triangles up), and 80T11 (circles) and the two peaks of cryolite phase (crosses). The solid curves are parabolic fits of the initial evolutions by using $\Delta S/S_0 = [(NT_r)^2 M_2^{\text{FNa}}]/[I(I+1)\pi^2]$ where M_2^{FNa} is the second moment. Error bars are drawn for $\Delta S/S_0 \leq 0.2$.

peak related to AlF_6^{3-} environments includes more than 80% of the aluminum atoms in this phase (Table 2) for all ternary mixtures but glassy 80T11. The broad components evidenced around 65, 35, and 2 ppm are characteristic of disordered 4-, 5- and 6-fold coordinated aluminum environments found in aluminoborate glasses,^{14–17} possibly fluorinated to some degree. The amorphous component corresponding to Al^{IV} species present in the $[\text{Na}_3\text{AlF}_6-\text{TiO}_2]_{11}$ mixture (“0T11”) changes upon addition of $\text{Na}_2\text{B}_4\text{O}_7$ because its isotropic chemical shift ($\delta_{\text{iso}}(\text{Al}^{\text{IV}})$) decreases from 81 to 67.5 ppm with an increasing amount of Al^{IV} units upon addition of $\text{Na}_2\text{B}_4\text{O}_7$. The reported $\delta_{\text{iso}}(\text{Al}^{\text{IV}})$ of sodium aluminoborate glasses¹⁵ lies in the 67–74 ppm range, and hence, our case represents mostly AlO_4^- units. For Al^{V} species, the value of 35.5 is found to be lower than the 36–45 ppm range found for aluminum pentacoordinated by oxygens in aluminoborate glasses.¹⁵ Because $\delta_{\text{iso}}(\text{AlF}_5^{2-})$ is 20 ppm,⁷ substitution of oxygen by fluorine is expected to lower the $\delta_{\text{iso}}(\text{AlO}_5)$, suggesting the presence of the oxyfluoro-species $\text{Al}(\text{O},\text{F})_5$ formed according to



The increasing Al^{IV} population with $\text{Na}_2\text{B}_4\text{O}_7$ content illustrated in Figure 1c shows the progressive ability of the borate matrix to keep in the solid state the Na_3AlF_6 initially dissolved in the high-temperature liquid.

The additional peak noticed at -0.3 ppm in 80T11 can be linked to the presence of Al^{VI} species, which are found in sodium aluminoborate glasses in the 8–15 ppm range. Similar to the Al^{V} case where the chemical shift of the aluminum coordinated by fluorine is more shielded than that of aluminum in pure oxygen environments, this downward shift of the δ_{iso} points to an oxygen–fluorine substitution in the first aluminum coordination sphere (see eq 1) or the presence of Ti in the vicinity of the AlO_6^{3-} species leading to

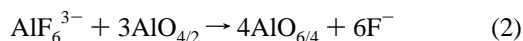


TABLE 3: Calculated and Experimental Second Moments and Calibration Factor Obtained from Various Atomic Configurations and REDOR Experiments

sample	$d_{\text{av}}(\text{X}-\text{F})$ Å	$M_2^{\text{calc}} (10^9)$	$M_2^{\text{exp}} (10^9)$	f
$\text{Na}_3\text{AlF}_6-\text{NaF}_6$	2.257	31.3	786×10^{-3}	25.1×10^{-3}
$\text{Na}_3\text{AlF}_6-\text{NaF}_8$	2.505	26.5	694×10^{-3}	26.1×10^{-3}
$\text{NaO}_{(6-n)}\text{F}_n$	2.250	$5.31 \times n$		
$\text{NaO}_{(8-n)}\text{F}_n$	2.500	$2.82 \times n$		
80T11		4.883	125×10^{-3}	25.6×10^{-3}
60T11		2.197	5.63×10^{-3}	25.6×10^{-3}
40T11		2.131	5.46×10^{-3}	25.6×10^{-3}
20T11		3.928	101×10^{-3}	25.6×10^{-3}
$\text{NaBF}_4-\text{BF}_4$	1.389	564		
$\text{BO}_{(4-n)}\text{F}_n$	1.390	$140 \times n$		
$\text{BO}_{(3-n)}\text{F}_n$	1.290	$220 \times n$		
$\text{B}-\text{O}-\text{Al}-\text{F}$	3.000	1.4		
$\text{NaBF}_4-\text{BF}_4$			1.01	
80T11- B^{IV}			0.151	
60T11- B^{IV}			0.110	
40T11- B^{IV}			0.100	
20T11- B^{IV}			0.0968	
80T11- B^{III}			0.103	
60T11- B^{III}			0.0652	
40T11- B^{III}			0.0575	
20T11- B^{III}			0.0571	

Moreover, unreacted AlF_6^{3-} ions (with respect to eq 2) seem to be trapped in a more distorted and distributed environment than the one found in cryolite, considering the increase of line width and reduced quadrupolar frequency of their related line.

It is also possible to apply the four-component model simulation of the 80T11 spectrum (see Figure 1 and Table 2) to simulate the 80B spectrum ($80\text{Na}_2\text{B}_4\text{O}_7:20\text{Na}_3\text{AlF}_6$) previously³ modeled with only two components. The result (not shown) is fully satisfactory and leads to the same overall spectral feature except for the relative populations of the Al^{IV} , Al^{V} , and Al^{VI} species. This similarity between the binary and ternary glasses with identical $\text{Na}_2\text{B}_4\text{O}_7$ content supports indirectly the glass former role played by TiO_2 when added in a small amount (2.6%) and pointed out in our previous IR and Raman investigation.⁹ Or, in other words, the highest field strength cation Ti^{4+} does not compete for fluorine atoms with boron and aluminum atoms when its content is relatively low in contrast with its behavior in 0T11.

Due to the overall small amount of aluminum contained in the samples, no MQMAS or even REDOR-like experiments could be performed.

Sodium-23. Figure 2a shows the ^{23}Na MAS NMR spectra of all the compositions investigated. The two peaks at 1.0 ppm ($C_{Q,\eta} = 600$ kHz) and -8.1 ppm ($C_Q = 1400$ kHz, $\eta = 0.2$) with a 1:2 ratio can easily be assigned to the crystalline cryolite phase known to be present in all samples except for 80T11 where cryolite seems to be completely inserted in the glassy matrix. This phase accounts for 90 to 33% of the total intensity of the spectrum, the remaining intensity belonging to a third broad feature. This third component can be successfully simulated using a second-order quadrupolar line shape including a distribution of quadrupolar parameters and an isotropic chemical shift in a procedure similar to the one used for ^{27}Al spectra and corresponds to the sodium atoms contained in the aforementioned glassy phase. The result of the simulation, as seen in Figure 2b, is very satisfactory with addition of a new small and narrow peak, accounting for a few percent of the total intensity that cannot be assigned at this stage of our study.

The main difference between the spectra of the various compositions lies therefore only in the relative proportion of

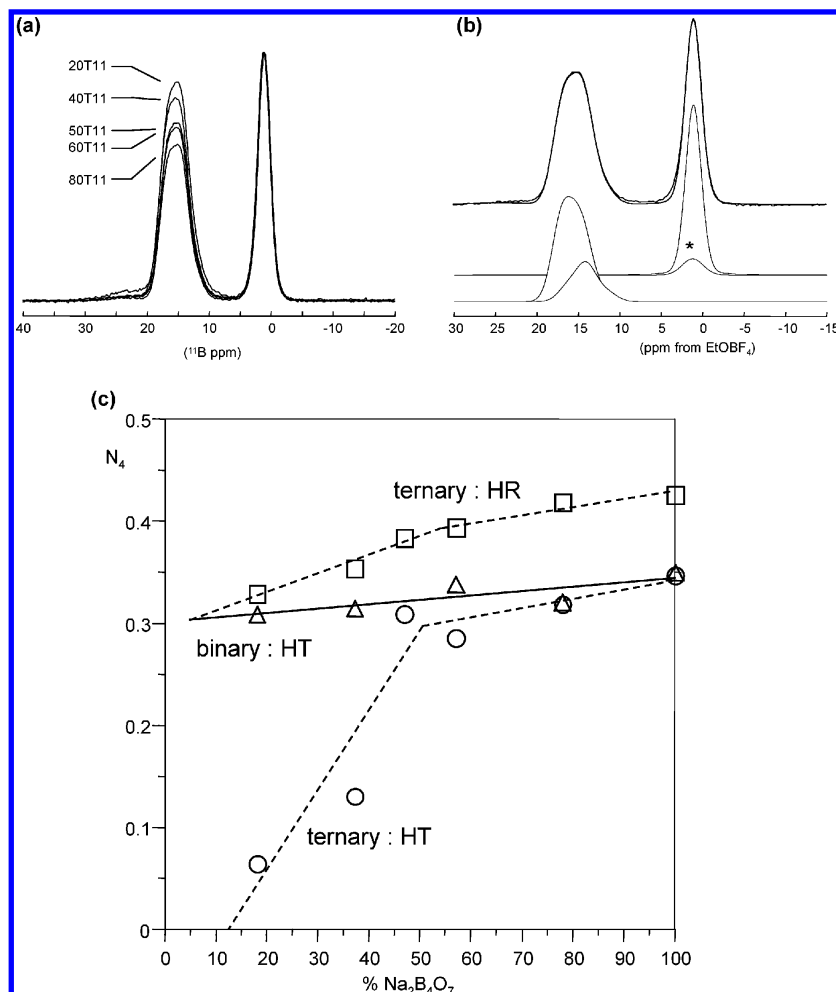


Figure 4. (a) One-pulse ^{11}B MAS NMR spectra of $\text{Na}_2\text{B}_4\text{O}_7$ – $[\text{Na}_3\text{AlF}_6\text{–TiO}_2]_{11}$ mixtures. (b) Spectrum and simulation for 60T11. (c) Comparative evolution of N_4 against $\text{Na}_2\text{B}_4\text{O}_7$ content for solid (squares) and molten (circles) $\text{Na}_2\text{B}_4\text{O}_7$ – $[\text{Na}_3\text{AlF}_6\text{–TiO}_2]_{11}$ mixtures as well as for the molten $\text{Na}_2\text{B}_4\text{O}_7$ – Na_3AlF_6 mixtures (triangles). Linear regressions are only a guide for the eyes.

the glassy phase component with respect to the cryolite one illustrated in Figure 1c. Within the 0T11–60T11 range, the sodium content in the $\text{Na}_2\text{B}_4\text{O}_7$ phase is found to be independent of the composition, as reflected by the unitary slope of the noticeable linear evolution (Figure 1). This behavior, somehow contrasting with the one previously mentioned for aluminum, points out a different mechanism of insertion of those two cations, Al^{3+} and Na^+ , into the borate matrix.

The $\{^{19}\text{F}\}^{23}\text{Na}$ REDOR curves, displayed in Figure 3, evidence a markedly steeper initial slope for the cryolite component compared to the glassy phase ones. Two distinct initial slopes are visible among the four compositions investigated: 80T11 and 20T11 on one side and 60T11 and 40T11 on the other. Although long evolution times were not accessible due to the short ^{23}Na spin–spin relaxation times ($T_2 \sim 12$ ms), one can follow the methodology developed by Eckert's group^{11,18} and concentrate on short evolution times, $\Delta S/S_0 < 0.2$, which exhibit a parabolic trend with a curvature dependent on the heteronuclear second moment, M_2^{IS} , as following

$$\frac{\Delta S}{S_0} = \frac{f}{I(I+1)\pi^2} (NT_r^2) M_2^{\text{IS}} \quad (3)$$

where $I = 1/2$ (the non-observed nucleus is ^{19}F), $S = 3/2$ (the observed nucleus is ^{23}Na), f is a calibration factor, and NT_r stands

for the duration of one rotor period multiplied by the number or rotor cycles. Hence, the van Vleck moment¹⁹ takes the form

$$M_2^{\text{IS}} = \frac{4}{15} \left(\frac{\mu_0}{4\pi} \right)^2 \gamma_I^2 \gamma_S^2 \hbar^2 I(I+1) \sum_I \frac{1}{r_{\text{IS}}^6} \quad (4)$$

where r_{IS} is the I–S internuclear distance (averaged over the vibrational motions) and the sum runs over all I atoms present in the crystal; the other symbols have their usual meanings.

Considering only the first coordination sphere or short range order, eq 4 enables us to evaluate M_2^{calc} for the two distinct environments present in Na_3AlF_6 . The resulting values are shown in Table 3 along with the M_2^{exp} obtained from the experimental REDOR curves through eq 3 (with $f = 1$). The calibration factor f is required for the agreement of M_2^{exp} with M_2^{calc} . In this table, M_2^{calc} values are given for simple configurations like NaO_5F , NaO_4F_2 , NaO_7F , and NaO_6F_2 using typical Na–F distances found in crystalline fluorides as well as the experimental values obtained for 80T11, 60T11, 40T11, and 20T11. The recalculated second moment uses the f value obtained for cryolite. Small values ($M_2^{\text{calc}} \sim 2.2$) for 60T11 and 40T11 are consistent with the presence of mainly NaO_7F species, which produce the smallest M_2^{calc} (~ 2.8). For 20T11 and 80T11, a more fluorinated species is required by the higher M_2^{calc} values: 3.9 and 4.9, respectively. Keeping an 8-fold

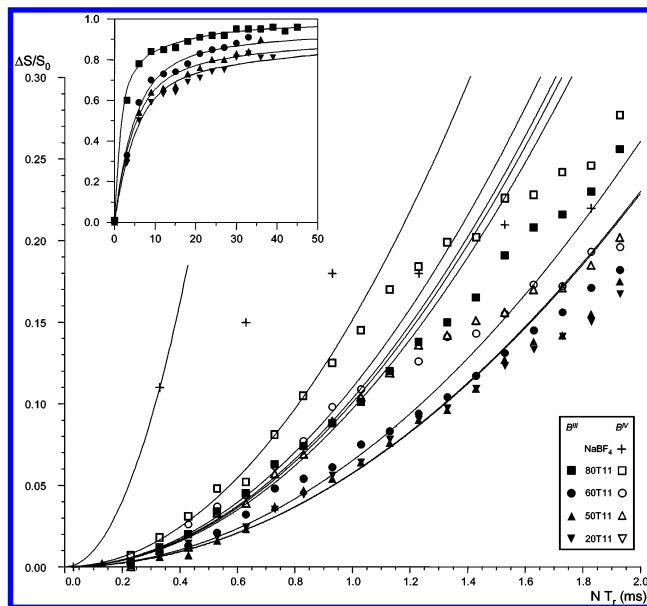


Figure 5. $\{^{19}\text{F}\}\{^{11}\text{B}\}$ REDOR curves for 20T11 (triangles down), 60T11 (circles), and 80T11 (squares) samples. B^{III} evolutions are represented by opened symbols and B^{IV} by filled ones. Lines are linear or parabolic fits through the first points (see text for details). The onset represents the same curve over longer evolution periods.

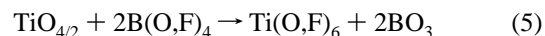
coordination state, NaO_6F_2 is the only possibility, but by no means can the lower coordination states $\text{NaO}_{7-x}\text{F}_x$ or $\text{NaO}_{6-x}\text{F}_x$ ($x = 1$ or 2) be ruled out. The surprising lowering of M_2^{calc} for intermediate compositions could actually be due to interplay between a change in sodium coordination number and in fluorine content. The sodium environment in NaBF_4 is NaF_8 , and in the two Na-bearing oxyfluoroborate crystals with known structures²⁰ are $\text{Na}(\text{O},\text{F})_6$ and $\text{Na}(\text{O},\text{F})_9$ for NaBF_3OH and NaO_2F_4 , NaO_2F_6 , and NaO_4F_4 for $\text{NaBeBO}_3\text{F}_2$. These findings might suggest that $\text{Na}(\text{O},\text{F})_8$ species can easily be found in oxyfluoroborates with a higher fluorine content. Because 20T11 is the mixture with the highest $[\text{F}]/([\text{F}] + [\text{O}])$ ratio in the glassy phase, one could then expect species like NaO_6F_2 and NaO_7F to be present, the proportion of the latter one increasing with $\text{Na}_2\text{B}_4\text{O}_7$ content at the expense of the former one. At the same time, a decrease in sodium coordination number would lead to the formation of NaO_6F and NaO_5F with a maximum amount in 80T11 because the $\text{Na}_2\text{B}_4\text{O}_7$ crystal is made of NaO_6 environments (with $d(\text{NaO}) = 2.499 \text{ \AA}$) and the diffraction techniques^{21,22} inferred in glassy sodium diborate a coordination number between 5 and 6.

These two competing mechanisms involving exchange between NaO_6F_2 and NaO_7F on one hand (at low $\text{Na}_2\text{B}_4\text{O}_7$ concentration) and formation of NaO_6F or NaO_5F on the other hand would then explain the observed behavior of the sodium van Vleck heteronuclear dipolar second moment.

Boron-11. Boron spectra of the ternary compositions between 20T11 and 80T11 (Figure 4a) recorded at 17.6 T show two very clear, distinguished signals, one for the 3-fold B^{III} sites (around 15 ppm) and the other for the 4-fold B^{IV} sites (around 0 ppm).^{23,24} As expected from XRD,⁹ no crystalline borate phase can be observed and all signal intensity comes from the glassy phase present in the samples leading to broad and featureless ^{11}B lineshapes. The main difference between the various compositions lies in the $[\text{B}^{\text{IV}}]/[\text{B}^{\text{III}}] = N_4/N_3 = N_4/(1 - N_4)$ ratio, which points to a change in chemical composition (and hence structure) of this sodium borate-based glass.²⁵ A simple calculation of N_4 based on a direct integration of those two components would neglect the intensity arising from the $n = 0$

spinning sideband of the external $-3/2, 3/2\rangle$ transition and hence lead to an error on the order of a few percent. If a Gaussian line shape has long been recognized to be successful for the B^{IV} signal, the simulation of the second-order quadrupolar broadened line shape resulting from a distribution of B^{III} sites is still a matter of debate. Using the previously mentioned second-order quadrupolar based model involving a Gaussian distribution of C_Q and δ_{iso} (see ^{27}Al and ^{23}Na), we found that a single component did not prove to be satisfactory; consequently, we performed the simulation with two. Even though it is tempting to assign those two components to two different boron environments such as ring and non-ring¹⁷ sites or oxyfluorospices,²⁶ it has to be considered at this stage of our study only as a tool to extract a precise value of N_4 .

This three-component model displayed in Figure 4b leads then to the following NMR parameters. For $\text{B}^{\text{III}}_{\text{a}}$: $\delta_{\text{iso}} = 17.4 \text{ ppm}$, $C_Q = 2.41 \text{ MHz}$, $\eta_Q = 0.9$. For $\text{B}^{\text{III}}_{\text{b}}$: $\delta_{\text{iso}} = 18.6 \text{ ppm}$, $C_Q = 2.59 \text{ MHz}$, $\eta_Q = 0.2$. For B^{IV} : $\delta_{\text{iso}} = 1.2 \text{ ppm}$, $C_{Q,\eta} = 0.4 \text{ MHz}$ (obtained by a SORGE procedure),¹² $\Delta\nu_{1/2} = 550 \text{ Hz}$. This set of parameters allows us to simulate all of the ^{11}B spectra, and only the intensities of those components are found to be sensitive to the composition. For pure $\text{Na}_2\text{B}_4\text{O}_7$ glass, we then found $N_4 = 0.43$, in excellent agreement with previous measurements,²⁵ and $N_4 = 0.42, 0.39, 0.38, 0.35$, and 0.33 for 80T11, 60T11, 50T11, 40T11, and 20T11, respectively. This evolution as a function of the $\text{Na}_2\text{B}_4\text{O}_7$ content is displayed in Figure 4c and evidences different behaviors between TiO_2 -rich and TiO_2 -poor compositions, in agreement with our prior IR study.⁹ A possible mechanism to enhance the conversion of B^{IV} into B^{III} occurring in the TiO_2 -rich region (and low $\text{Na}_2\text{B}_4\text{O}_7$ content) could be the Ti coordination change:



of less importance within 60–90% $\text{Na}_2\text{B}_4\text{O}_7$, where Na_3AlF_6 plays the glass modifier role.

To evidence the boron–fluorine connectivity, we also performed $\{^{19}\text{F}\}\{^{11}\text{B}\}$ REDOR experiments on 20T11, 50T11 (data not shown but extremely similar to 20T11), 60T11, and 80T11 (Figure 5). Because B^{IV} sites presented very short T_2 values (about 3.5 ms), long evolution times could be obtained only for B^{III} , as seen in the onset in Figure 5 but are still limited in time ($T_2(\text{B}^{\text{III}}) \sim 20 \text{ ms}$). It is nevertheless obvious from this graph that the REDOR effect (steepness of the initial evolution) increases and that the curves level off at higher values upon increasing the $\text{Na}_2\text{B}_4\text{O}_7$ content. This can be explained by an increase of the overall fluorine content in the glassy borate phase, i.e., an increased solubility of $[\text{Na}_3\text{AlF}_6\text{--TiO}_2]_{11}$, or the formation of free F^- ions at low $\text{Na}_2\text{B}_4\text{O}_7$ concentration.

Removing the very first points influenced by the ^{11}B background signal, a parabolic fit seems reasonable for all sites for $\Delta S/S_0 < 0.1$ (a limiting value lower than the 0.2 or 0.3 one usually uses).^{11,18} The reference compound available to us, NaBF_4 , contains only B^{IV} sites that display REDOR curves very quickly affected by the F–F homonuclear couplings. Thus, the influence of the spinning speed and of the strong damping of the REDOR effect prevented us from performing a quantitative analysis. We can nevertheless note qualitative trends: (1) for all compositions, the boron van Vleck heteronuclear dipolar second moment is bigger for B^{IV} sites than for B^{III} sites, and (2) it stays rather constant in the 20–60% $\text{Na}_2\text{B}_4\text{O}_7$ range and markedly increases for 80T11. However, the former trend is not intuitive because on average the B–F distance is bigger in BO_3F species than in BO_2F ones, leading to smaller $M_2^{\text{B–F}}$ values (see Table 3 for typical values). This then suggests the

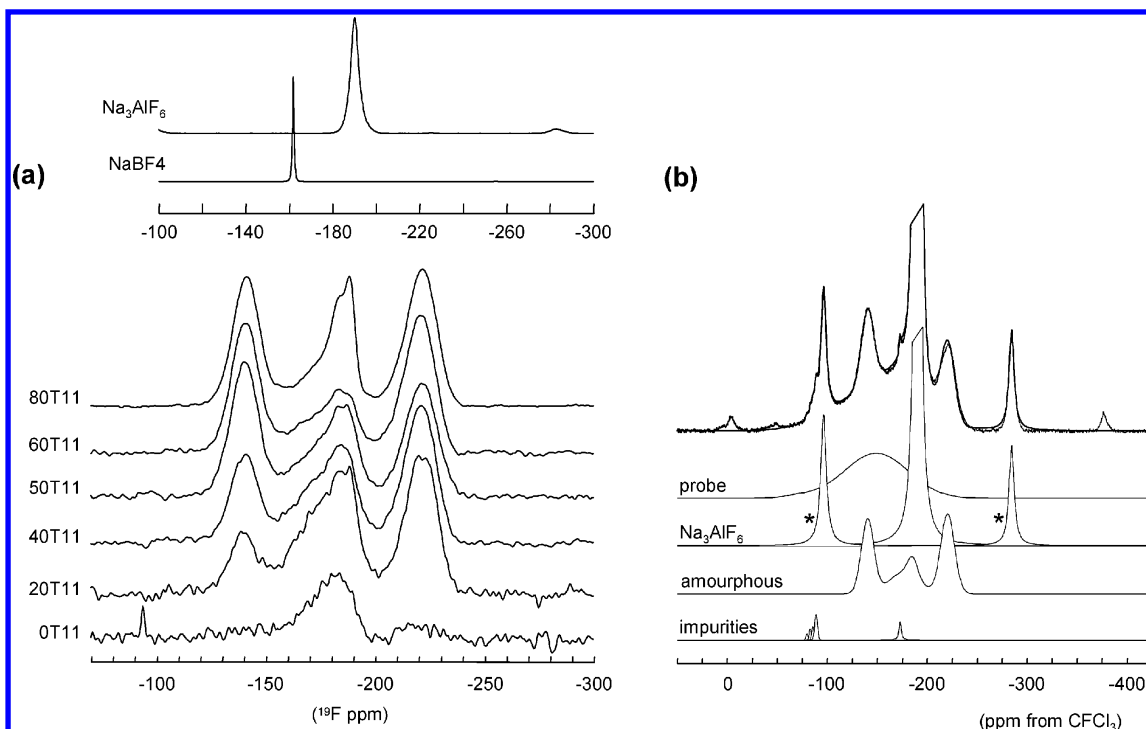


Figure 6. (a) ^{19}F Hahn-echo MAS NMR spectra of $\text{Na}_2\text{B}_4\text{O}_7$ - $[\text{Na}_3\text{AlF}_6\text{-TiO}_2]_{11}$ mixtures compared with the spectra of reference crystalline compounds: Na_3AlF_6 and NaBF_4 . (b) Simulation of one-pulse ^{19}F spectrum for 60T11.

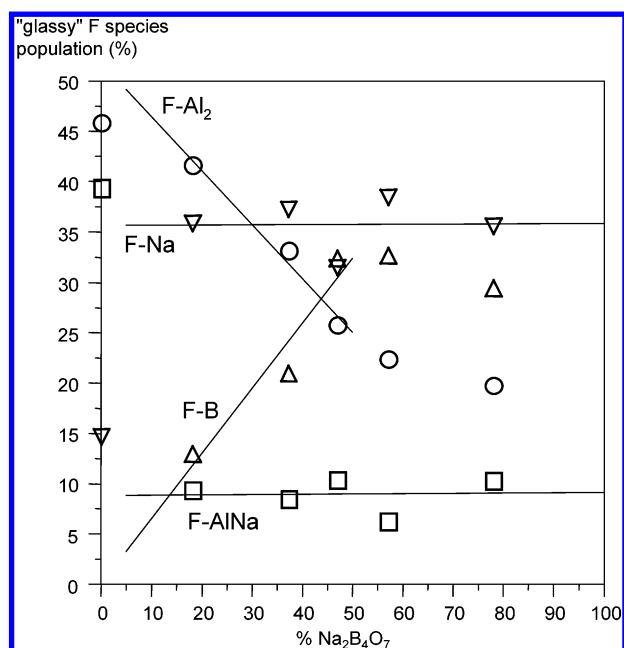
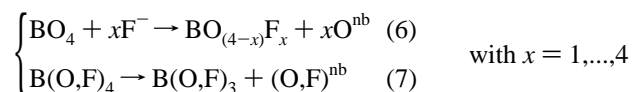


Figure 7. Population of the four F species in the ^{19}F spectra; lines are guides for the eyes only.

presence of BO_2F_2 along with BO_3F and BO_2F species in all but the 80T11 sample. This behavior is consistent with the fluorine preference for higher field-strength cations²⁸ (B^{III} having a smaller atomic radius than B^{IV}).

Similarly, increase of the $M_2^{\text{B-F}}$ values for 80T11 points out presence of the BOF_2 species as well as an increased amount of BO_2F_2 . The absence of Ti^{4+} (identified as TiO_4 units)⁹ for fluorine competition allowed the formation of higher fluorinated environments of borons. This behavior is strengthened by the increased content of F atoms in the borate matrix following the complete dissolution and the advanced decomposition of cryolite. Hence, weakening of the glassy borate network takes place

by either substitution of O^{2-} by F^- or by conversion of oxyfluoro- B^{IV} species into F^{nb} -bearing B^{III} according to



(where nb stands for "nonbridging"). No completely fluorinated environments of boron were depicted.

Fluorine-19. The cryolite component present in all but 80T11 compositions produces in the ^{19}F MAS spectra a strong peak located at -190 ppm with associated spinning sidebands. This line and the unavoidable ^{19}F background signal obscure smaller features in all spectra. We took advantage of their short T_2^* , due to respectively residual ^{19}F - ^{19}F homonuclear dipolar coupling and field inhomogeneity, to remove them by performing Hahn-echo experiments at a long evolution time. These T_2 -filtered experiments shown in Figure 6a allow us to access the fluorine environments in the borate glassy phase (i.e., experiencing weak ^{19}F - ^{19}F homonuclear couplings averaged out by spinning at 35 kHz). Relative intensities of the various peaks were checked to be independent of the selected evolution time. Three broad lines centered around -140 , -180 , and -220 ppm are then clearly evidenced along with the central one being split into two components. All T_2 -filtered spectra can therefore be simulated by a set of four Gaussian lines located at -140.0 , -176.5 , -186.0 , and -220.5 ppm with full width at half-maximum ($\Delta\nu_{1/2}$) of 5.65, 11.5, 4.5, and 6.2 kHz, respectively. The relative intensity of each component is the only parameter affected by the composition.

Because the position of the peak located at -220.5 ppm is close to $\delta(\text{FNa}_6) = -221$ ppm in NaF, one can assign this component to free F-Na_z configurations (with $z \sim 6$).^{27,28} On the basis of the observed ^{19}F peak positions in alkali-fluoroaluminate systems,⁵ we can also attribute the peak located at -186 ppm to Al-F-Na_z environments; the one at -176.5 ppm is related to the presence of Al-F-Al species. There is

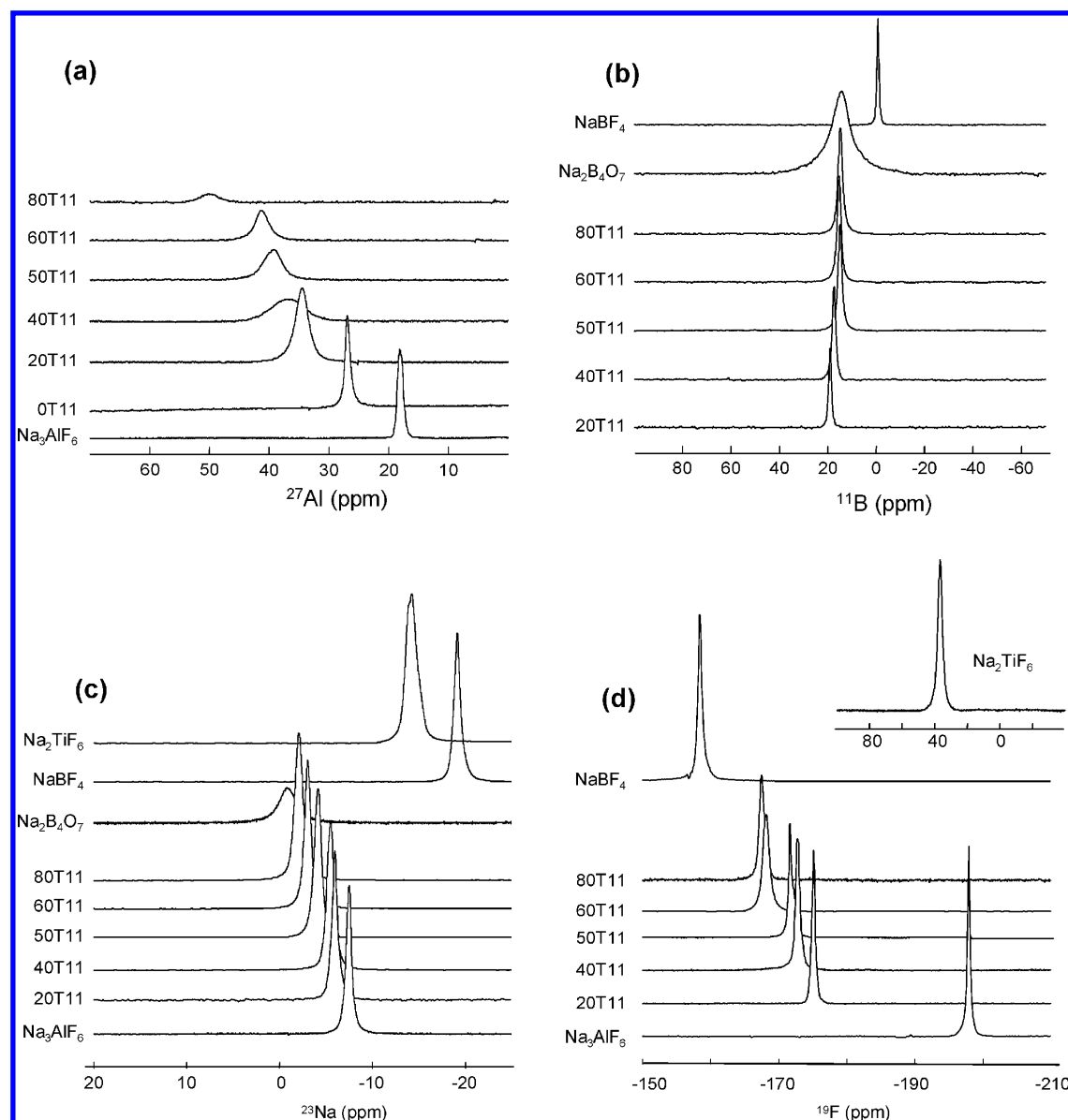


Figure 8. High-temperature NMR spectra of the $\text{Na}_2\text{B}_4\text{O}_7$ -[Na_3AlF_6 - TiO_2]₁₁ mixtures: (a) ^{27}Al , (b) ^{11}B , (c) ^{23}Na , (d) ^{19}F .

nevertheless some uncertainty with this latter assignment because this broad peak overlaps with regions where $\text{BF}_3\text{F}-\text{Na}_x$ species are expected ($\delta(\text{BF}_3\text{FNa}_2) = -162$ ppm in NaBF_4). To our best knowledge, the only ^{19}F chemical shift investigation in oxyfluoroborate glasses²⁶ has evidenced the following positions: $\delta(\text{F}-\text{BO}_2) = -115$ ppm, $\delta(\text{F}-\text{BOF}) = -139$ ppm, and $\delta(\text{F}-\text{BO}_2\text{F}) = -121$ ppm (bridging F). The peak located at -140 ppm is therefore clearly assigned to $\text{F}-\text{B}(\text{O},\text{F})_x$ (with $x = 2, 3$). The very likely unit is $\text{F}-\text{BOF}$ (in agreement with our prior $\{^{19}\text{F}\}^{11}\text{B}$ REDOR findings), but the unknown influence of the nearby Na or Ti atoms on the ^{19}F chemical shifts prevents us from getting into more details. Finally, an additional narrow peak centered around -188.7 ppm and accounting for less than 5% of the total intensity is observed in 80T11 spectra and readily assigned to cryolite-like isolated $\text{F}-(\text{AlF}_6)\text{Na}_3$ fluorine environments associated with the very first step of its recrystallization.

Using the experimental T_2 -filtered spectra as a component of the quantitative one-pulse experiment simulation, we retrieved the evolution of the glassy phase population illustrated in Figure 1c. A similar behavior to aluminum is observed; i.e., the progressive dissolution of Na_3AlF_6 in the borate matrix is linear with the $\text{Na}_2\text{B}_4\text{O}_7$ content, but the slope of this trend is far less

than 1, as would predict a perfect mixing case; F^- ions might therefore enter the borate matrix with Al^{3+} as counterions. Within the glassy phase, evolution of the fluorine speciation with composition (Figure 6c) indicates no modification of the proportion of the FNa_x and FAlNa_x species over the whole compositional range. In contrast, the amount of bridging $\text{Al}-\text{F}-\text{Al}$ decreases markedly, and the proportion of $\text{F}-\text{B}$ environments increases within 20–50% $\text{Na}_2\text{B}_4\text{O}_7$. In other words, oxyfluoroborate species are formed at the expense of the aluminate ones according to eqs 1 and 6. This is again consistent with the aforementioned fluorine preference for higher field-strength cations (i.e., B^{3+} over Al^{3+} in this case). Above 50% $\text{Na}_2\text{B}_4\text{O}_7$, the fluorine atoms tend to be randomly distributed over all possible sites because no significant evolution of the fluorine speciation is observed.

The question of the presence of oxyfluorotitanium species is partially addressed here because no signal is detected around the region where the ^{19}F resonance of Na_2TiF_6 appears (i.e., 40 ppm), and therefore, no $\text{Ti}^{\text{IV}}-\text{F}-\text{Na}_2$ is expected over the whole range of composition studied. Given the fact that neither $\text{Al}-\text{F}-\text{Ti}$ or $\text{B}-\text{F}-\text{Ti}$ species were reported by NMR studies up to now, it is difficult to completely discard the presence of

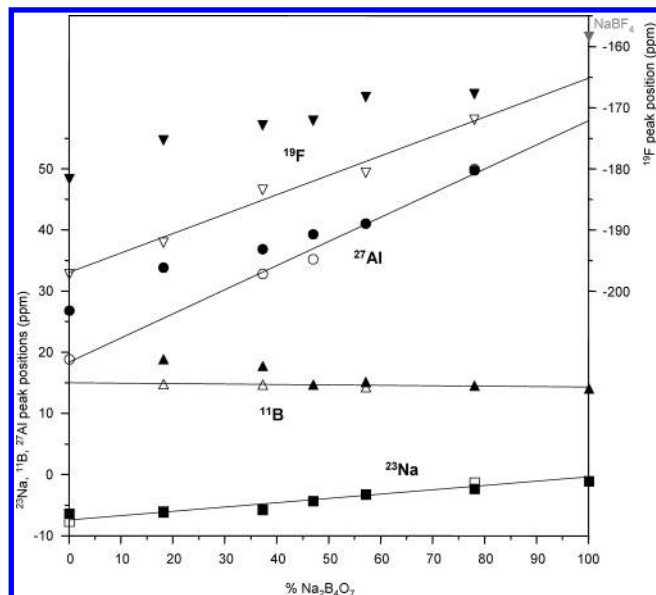


Figure 9. Peak position variation of high-temperature NMR spectra as a function of composition: Squares, ^{23}Na ; circles, ^{27}Al ; triangles up, ^{11}B ; triangles down, ^{19}F . Full symbols refer to the ternary system $\text{Na}_2\text{B}_4\text{O}_7$ – $[\text{Na}_3\text{AlF}_6\text{–TiO}_2]_{11\%}$ whereas opened ones refer to the binary $\text{Na}_2\text{B}_4\text{O}_7$ – Na_3AlF_6 .³ Straight lines are linear regressions performed on the binary composition values.

oxyfluorotitanium environments especially if we consider the important width of the lines involved in these spectra. However, the absence of any strong component related to F–Ti bonds suggests a bonding preference of Ti for oxygen rather than fluorine.

3.2. In Situ High-Temperature NMR. ^{27}Al , ^{23}Na , ^{11}B , and ^{19}F high-temperature NMR spectra of all investigated melts are displayed on Figure 8 along with some reference compounds also obtained in the molten phase. All spectra consist of a single Lorentzian line due to the very fast (on NMR time scale) chemical exchange between the various species present in the melts. The positions of these lines are therefore the population-weighted averaged of each individual isotropic chemical shift of the species present in the melt and are therefore sensitive to the nature of these entities and their relative proportion. The evolution of these parameters as a function of composition is shown on Figure 9 for all investigated nuclei, and the numerical values are summarized in Table 4.

Aluminum-27. As seen from Figure 8a, addition of 11% TiO_2 in pure Na_3AlF_6 (i.e., sample “0T11”) results in a peak shift from 19 to 28 ppm. Then, upon addition of $\text{Na}_2\text{B}_4\text{O}_7$, the ^{27}Al peak position increases slowly to 41 ppm for 80% $\text{Na}_2\text{B}_4\text{O}_7$ (Figure 9), a behavior similar to that observed³ for the binary system Na_3AlF_6 – $\text{Na}_2\text{B}_4\text{O}_7$ and a value that can be compared to the average one of 22.6 ppm calculated from the values in Table 2 obtained for that same composition (i.e., 80T11). This is in contrast with high-temperature ^{27}Al NMR results obtained on a lithium boroaluminate composition²⁹ and shows that the AlF_6 species accounting for 26% in solid 80T11 is not to be expected in the high-temperature liquid that is chemically more homogeneous than its corresponding quenched sample.

Two mechanisms strongly affecting the aluminum chemical shift can take place in the melt: (a) oxyfluoro-species formation according to reaction 1 and (b) modification of the average coordination number of aluminum by changing the relative proportions of Al^{IV} , Al^{V} , and Al^{IV} species. The first mechanism is mainly responsible for the positive 9 ppm shift observed upon

addition of TiO_2 into pure Na_3AlF_6 (i.e., sample “0T11”) and corresponds to the formation of oxyfluoro-aluminated species as it has been already observed in the case of Al_2O_3 additions in molten cryolite.⁷ In contrast, evolution with increasing $\text{Na}_2\text{B}_4\text{O}_7$ content for both ternary and binary compositions might reflect a decrease of the average aluminum coordination number. With respect to the similar binary Na_3AlF_6 – $\text{Na}_2\text{B}_4\text{O}_7$ compositions, addition of TiO_2 within 0–50% $\text{Na}_2\text{B}_4\text{O}_7$ leads to a lower average coordination state of aluminum, a behavior consistent with the formation of octahedral titanium species as observed in our previous IR study.⁹

Boron-11. The single Lorentzian lines observed for all compositions (Figure 8b) are the result of the chemical exchange taking place between the B^{III} and B^{IV} species. Their positions’ δ_{iso} is therefore the average between the positions δ^{III} and δ^{IV} corresponding to these two environments weighted by their respective population N_3 and N_4 :

$$\delta_{\text{iso}} = N_3\delta^{\text{III}} + N_4\delta^{\text{IV}} \quad \text{with } N_3 = 1 - N_4 \quad (8)$$

Because our study showed no dependence with composition of either B^{III} or B^{IV} peak position in the solid-state, we can make the same assumption for the high-temperature liquid values and further postulate that

$$\begin{cases} \delta^{\text{III}} = 18 + \delta_0 \\ \delta^{\text{IV}} = 1 + \delta_0 \end{cases} \quad (9)$$

where numerical values have been taken from the solid-state results and δ_0 is a constant shift intended to account for temperature effects. Combining eqs 8 and 9, one straightforwardly gets from each high-temperature ^{11}B line position δ

$$N_4 = \frac{(\delta - \delta^{\text{III}})}{(\delta^{\text{IV}} - \delta^{\text{III}})} = (18 + \delta_0 - \delta)/17 \quad (10)$$

Recalling that neutron diffraction studies^{31,32} have shown that $N_4 = 0.35$ for $\text{Na}_2\text{B}_4\text{O}_7$ at 1000 °C, we get $\delta_0 = 2.15$ ppm from our experimental value at 980 °C and can then use eq 10 to evaluate N_4 for the other compositions giving 0.32, 0.29, 0.31, 0.13, and 0.06 for 80T11, 60T11, 50T11, 40T11, and 20T11, respectively.

All values are significantly smaller than the ones obtained using the solid-state experiments, evidencing again that a direct correlation between the structure of the (partially crystallized) quenched samples and their corresponding melts is hazardous. N_4 is found to increase sharply in the low 0–50% $\text{Na}_2\text{B}_4\text{O}_7$ content (see Figure 4c) as a consequence of the aforementioned change in titanium coordination (eq 5) prevailing in this compositional range. This influence on the structure of the $\text{Na}_2\text{B}_4\text{O}_7$ melt is further evidenced by the monotonous behavior of N_4 in the Ti-free case of the Na_3AlF_6 – $\text{Na}_2\text{B}_4\text{O}_7$ system. Above 50% $\text{Na}_2\text{B}_4\text{O}_7$, N_4 values for the ternary compositions are reaching those of the binary one as a consequence of the modifier role played by Na_3AlF_6 in this compositional range.

Sodium-23. As noticed in Figure 8c, starting from a purely fluorinated environment of cryolite (NaF_6 , $\delta = -7.5$ ppm), the sodium line position shifts to -6.2 ppm upon addition of TiO_2 and then evolves linearly toward its value of -1.0 ppm in pure $\text{Na}_2\text{B}_4\text{O}_7$ (see Figure 9). Because, for a given Na–(O,F) mean bond length, the sodium isotropic positions in oxides is known to lie systematically above those from fluoride,³³ substitution of fluorine by oxygen is expected to produce a positive shift. In contrast, changes in mean bond lengths can be observed

TABLE 4: High-Temperature NMR Results for ^{27}Al , ^{11}B , ^{23}Na , and ^{19}F Nuclei in All Compositions Investigated in the $\text{Na}_2\text{B}_4\text{O}_7\text{:}[\text{Na}_3\text{AlF}_6\text{--TiO}_2]_{11}$ System and Some Reference Compounds

sample	^{27}Al		^{11}B		^{23}Na		^{19}F	
	δ (ppm)	$\Delta\nu_{1/2}$ (Hz)	δ (ppm)	$\Delta\nu_{1/2}$ (Hz)	δ (ppm)	$\Delta\nu_{1/2}$ (Hz)	δ (ppm)	$\Delta\nu_{1/2}$ (Hz)
Na_3AlF_6	19.0	112			−7.5	69	−197.0	204
0T11	27.0	86			−6.2	296	−181.5	758
20T11	34.0	250	19.0	170	−6.0	66	−175.1	251
40T11	37.0	293	17.9	184	−5.5	94	−172.7	307
50T11	39.5	384	14.9	258	−4.2	104	−172.0	219
60T11	41.2	299	15.3	251	−3.0	78	−168.1	452
80T11	49.9	375	14.7	269	−2.2	92	−167.6	275
$\text{Na}_2\text{B}_4\text{O}_7$			14.2	612	−0.9	242		
NaBF_4			−0.7	122	−19.2	81	−158.2	261
Na_2TiF_6					−14.3	207	36.8	1187

between molten Na_2TiF_6 ($\bar{d}_{\text{solid}}(\text{NaF}_6) = 2.262 \text{ \AA}$) and NaBF_4 ($\bar{d}_{\text{solid}}(\text{NaF}_8) = 2.466 \text{ \AA}$) leading to peak positions of −14.2 and −19.2 ppm, respectively; i.e., increasing the coordination number produces a negative ^{23}Na line shift. This has also been found in molten sodium borates and germanates³⁴ where the peak frequency exhibits a slight decrease with increasing temperature due to a slight increase in the mean size of the sodium site. Because addition of $\text{Na}_2\text{B}_4\text{O}_7$ increases the sodium line position, the dominant mechanism at play here is the progressive substitution of fluorine by oxygen in the first coordination sphere of sodium.

It can be noticed that no significant differences in line position can be seen with respect to the values obtained in the binary system and hence that the averaged sodium environments do not seem to be affected by the presence of TiO_2 in the melt. This finding also points toward a bonding preference of fluorine toward sodium, leaving the majority of oxygen atoms linked to titanium. The high-temperature peak positions are also found to be reasonably close to the ^{23}Na isotropic chemical shifts obtained in the glassy phase of the quenched samples with values ranging from −8.0 (0T11) to −5.2 ppm (80T11). The environments depicted in the previous solid-state study can therefore, in first approximation, be seen as representative of those expected in the high-temperature liquid state.

Fluorine-19. The observed ^{19}F peak positions for the ternary melts are ranging from −181 to −168 ppm (Figure 8d) far away from the positions found in molten Na_2TiF_6 (36.8 ppm) and in between molten Na_3AlF_6 (−197.0 ppm) and molten NaBF_4 (−158.2 ppm). The influence of TiO_2 addition in the 0T11 melt is found to be shifted by 15.5 ppm with respect to Na_3AlF_6 . Given the fact that the fluorine line position is not influenced by the presence of oxygen,⁷ this positive shift can only be due to the formation of F–Ti bonds and its small amplitude strongly suggests that only a very small amount of these links are created in the melt. This is in agreement with the absence of signal arising from such environments in the quenched samples and expresses an oxygen bonding preference for titanium. As the concentration of TiO_2 lowers in melts (i.e., increasing $\text{Na}_2\text{B}_4\text{O}_7$ content), the probability of finding F–Ti bonds lowers as well and the ^{19}F chemical shifts behavior of the ternary melts tends to meet the ones observed for the binary $\text{Na}_3\text{AlF}_6\text{--Na}_2\text{B}_4\text{O}_7$ melts (Figure 4c).

For molten ternary and binary compositions, the extrapolated ^{19}F peak frequency at 100% $\text{Na}_2\text{B}_4\text{O}_7$ tends to reach values of −160 and −165 ppm, respectively, extremely close to the −158.2 ppm found in molten NaBF_4 . By analogy with the solid-state structure of this latter compound, fluorine environments in the $\text{Na}_2\text{B}_4\text{O}_7$ -rich melts can be thought as being mainly of F– $\{\text{BO}_{(3-x)}\text{F}_x\}\text{Na}_2$ -type. This preference toward F–B bonds instead of F–Al ones is consistent with the increasing F–B species population at the expense of F–Al₂ observed in the quenched samples upon increasing $\text{Na}_2\text{B}_4\text{O}_7$ content. Moreover,

on the basis of the solid-state study, the average ^{19}F isotropic chemical shift weighted by the various species population in 80T11 is −183.2 ppm, a value in good agreement with the high-temperature one taking into account shifts due to temperature effect and possible early stage of Na_3AlF_6 solidification.

4. Conclusions

Our multinuclear solid-state and high-temperature molten state investigation of the pseudo-binary $\text{Na}_2\text{B}_4\text{O}_7\text{--}[\text{Na}_3\text{AlF}_6\text{--TiO}_2]_{11}$ system enabled us to identify two distinct behaviors in accordance with the $\text{Na}_2\text{B}_4\text{O}_7$ content, below and above 50% $\text{Na}_2\text{B}_4\text{O}_7$. In the low $\text{Na}_2\text{B}_4\text{O}_7$ region, formation of B^{III} units at the expense of B^{IV} units was noticed, especially in molten phase and to a lesser extent in the quenched samples. Correlatively, addition of TiO_2 in the high-temperature melt leads to a lower average coordination state of aluminum atoms also observed in the glassy phase of the solidified samples. Both trends were supported by the predominance of the Ti^{IV} → Ti^{VI} valence conversion in this region. $\{^{19}\text{F}\}^{11}\text{B}$ and $\{^{19}\text{F}\}^{23}\text{Na}$ REDOR experiments have also evidenced the presence of oxyfluoro-species, mainly BO_2F_2 , BO_3F , and BO_2F on one hand and NaO_7F and NaO_6F_2 on the other. Presence of $\text{Al}(\text{O},\text{F})_5$ units in the quenched samples was inferred from ^{27}Al MAS spectra. More intricate evolution was depicted for the fluorine environments: F–Na and F–AlNa (with populations approximately constant over the whole compositional range) and F–Al₂ and F–B (the former being dominant at low $\text{Na}_2\text{B}_4\text{O}_7$ concentration and the population of the latter increasing at the expense of the F–Al₂).

Above 50% $\text{Na}_2\text{B}_4\text{O}_7$, cryolite inserted in the glassy diborate $\text{Na}_2\text{O} \cdot 2\text{B}_2\text{O}_3$ network plays a network former role as seen by the predominance of Al^{IV} species. Despite the fact that Ti⁴⁺ is a potential glass modifier, its reduced content does not alter considerably the B^{III}/B^{IV} speciation. These mixtures behave like those in $\text{Na}_3\text{AlF}_6\text{--Na}_2\text{B}_4\text{O}_7$ for rich $\text{Na}_2\text{B}_4\text{O}_7$. In the glassy part of the solidified samples, formation of lower coordination sodium state NaO_6F and NaO_5F is also expected from the $\{^{19}\text{F}\}^{23}\text{Na}$ REDOR experiments; its $\{^{19}\text{F}\}^{11}\text{B}$ counterpart points to an increased amount of BO_2F_2 and formation of BOF_2 borate species. The ^{19}F line positions in melts suggest that, at high $\text{Na}_2\text{B}_4\text{O}_7$ content, the fluorine atoms are preferentially found in a F– $\{\text{BO}_{(3-x)}\text{F}_x\}\text{Na}_2$ -type of configuration. Fluorine bonding preference for higher field-strength cations applies here in the whole range of composition, leading to preferential F–B rather than F–Al bondings, and F–B^{IV} rather than F–B^{III}. Moreover, if Ti–F bonds are expected in these liquids, their amount stays very reduced over the complete compositional range.

Thus, NMR findings strengthened our prior investigations carried out by vibrational spectroscopy (IR and Raman) of this system⁹ and described in more detail the species expected to be present in the high-temperature liquid-state. If the experi-

ments performed on the quenched samples yield more specific information than the in situ ones, one should nevertheless keep in mind that the tendency to crystallize Na_3AlF_6 and TiO_2 upon cooling does not allow the glassy phase present in those samples to be completely equivalent to the frozen liquid state. This is confirmed here by the ^{27}Al NMR investigation, which shows some discrepancies between the high-temperature liquid and the quenched structures. Despite its inherent technical difficulties and the apparent lack of details contained in the simple Lorentzian lineshapes, in situ experiments are a necessary step to access the structure of the complex melts.

Acknowledgment. This work has been financially supported by the EEC ARI contract HPRI-CT-1999-00042 and CNRS-Romanian Academy cooperation.

References and Notes

- (1) Gomes, J. N.; Ukida, K. U.S. Patent 3,775,271, 1972.
- (2) Makyta, M.; Danek, V.; Haarberg, M.; Thonstad, J. *J. Appl. Electrochem.* **1996**, 26, 319–324.
- (3) Bessada, C.; Anghel, E. M. *Inorg. Chem.* **2003**, 42, 3884–3890.
- (4) Stebbins, J. F. *Chem. Rev.* **1991**, 91, 1353–1373.
- (5) Stebbins, J. F.; Farnan, I.; Dando, N.; Tzeng, S. Y. *J. Am. Ceram. Soc.* **1992**, 75, 3001–3006.
- (6) Robert, E.; Lacassagne, V.; Bessada, C.; Massiot, D.; Gilbert, B.; Coutures, J.-P. *Inorg. Chem.* **1999**, 38, 214–217.
- (7) Lacassagne, V.; Bessada, C.; Florian, P.; Bouvet, S.; Ollivier, B.; Coutures, J.-P.; Massiot, D. *J. Phys. Chem. B* **2002**, 106, 1862–1868.
- (8) Gullion, T.; Schaefer, J. J. *Adv. Magn. Reson.* **1989**, 13, 57–83.
- (9) Anghel, E. M.; Florian, P.; Bessada, C. *J. Phys. Chem. B* **2007**, 111, 962–967.
- (10) Massiot, D.; Fayon, F.; Capron, M.; King, I.; Le Calvé, S.; Alonso, B.; Durand, J.-O.; Bujoli, B.; Gan, Z.; Hoatson, G. *Magn. Reson. Chem.* **2002**, 40, 70–76.
- (11) Bertmer, M.; Zuchner, L.; Chan, J. C. C.; Eckert, H. *J. Phys. Chem. B* **2000**, 104, 6541–6553.
- (12) Massiot, D.; Müller, D.; Hübert, T.; Schneider, M.; Kentgens, A. P. M.; Coté, B.; Coutures, J.-P.; Gessner, W. *Solid State NMR* **1995**, 5, 175–180.
- (13) Massiot, D.; Fayon, F.; Capron, M.; King, I.; Le Calvé, S.; Alonso, B.; Durand, J.-O.; Bujoli, B.; Gan, Z.; Hoatson, G. *Magn. Reson. Chem.* **2002**, 40, 70–76.
- (14) Simon, S.; van Moorsel, G. J. M. P.; Kentgens, A. P. M.; de Boer, E. *Solid State NMR* **1995**, 5, 163–173.
- (15) Zuchner, L.; Chan, J. C. C.; Müller-Warmuth, W.; Eckert, H. *J. Phys. Chem. B* **1998**, 102, 4495–4506.
- (16) Chan, J. C. C.; Bertmer, M.; Eckert, H. *J. Am. Chem. Soc.* **1999**, 121, 5238–5248.
- (17) Du, L.-S.; Stebbins, J. F. *Solid State NMR* **2005**, 27, 37–49.
- (18) Epping, J. D.; Strojek, W.; Eckert, H. *Phys. Chem. Chem. Phys.* **2005**, 7, 2384–2389.
- (19) van Vleck, J. H. *Phys. Rev.* **1948**, 74 (9), 1168–1183.
- (20) Inorganic Crystal Structure Database (ICSD); Fachinformationzentrum: Karlsruhe, Germany.
- (21) Paschina, G.; Piccaluga, G.; Magini, M. *J. Chem. Phys.* **1984**, 81, 6201–6206.
- (22) Swenson, J.; Börjesson, L.; Howells, W. S. *Phys. Rev. B* **1998**, 57 (21), 13514–13526.
- (23) Bray, P. J. *Inorg. Chim. Acta* **1999**, 289, 158–173.
- (24) Kroeker, S.; Stebbins, J. F. *Inorg. Chem.* **2001**, 40, 6239–6246.
- (25) Bray, P. J.; O'Keefe, J. G. *Phys. Chem. Glasses* **1963**, 4 (2), 37–46.
- (26) Boussard-Plédel, C.; Le Floch, M.; Fonteneau, G.; Lucas, J.; Sinbandhit, S.; Shao, J.; Angell, C. A.; Emery, J.; Buzaré, J. Y. *J. Non-Cryst. Solids* **1997**, 209, 247–256.
- (27) Kiczinski, T. J.; Du, L.-S.; Stebbins, J. F. *J. Non-Cryst. Solids* **2004**, 337, 142–149.
- (28) Kiczinski, T. J.; Stebbins, J. F. *J. Non-Cryst. Solids* **2002**, 306, 160–168.
- (29) Sen, S. *J. Non-Cryst. Solids* **1999**, 253, 84–94.
- (30) Dirken, J. D.; Jansen, J. B. H.; Schuiling, R. D. *Am. Mineral.* **1992**, 77, 718–724.
- (31) Majerus, O.; Cormier, L.; Calas, G.; Beuneu, B. *Phys. Rev. B* **2003**, 67, 4210–1–7.
- (32) Cormier, L.; Majerus, O.; Neuville, D. R.; Callas, G. *J. Am. Ceram. Soc.* **2006**, 89, 13–19.
- (33) Stebbins, J. F. *Solid State Ionics* **1998**, 112, 137–141.
- (34) George, A. M.; Sen, S.; Stebbins, J. F. *Solid State NMR* **1997**, 10, 9–17.